SUPPORTING INFORMATION

Engineering the compositional architecture of core-shell upconverting lanthanide-doped nanoparticles for optimal luminescent donor in resonance energy transfer : the effects of energy migration and storage

A.Pilch-Wrobel[1§], A.M.Kotulska[1§], S.Lahtinen[2], T.Soukka[2]*, A.Bednarkiewicz[1]*

[1] Institute of Low Temperature and Structure Research, PAN, ul. Okolna 2, Wrocław 50-422, Poland

[2] University of Turku, Department of Life Technologies/Biotechnology, Kiinamyllynkatu 10, 20520 Turku, Finland

[§] These authors contributed equally

Corresponding authors:

e-mail tero.soukka@utu.fi, Tel. +358 50 476 5571

e-mail a.bednarkiewicz@intibs.pl, Tel.+48 71 3954 192

TABLE OF CONCENT

1 MODELLING OF UC-FRET

1.1 INTRODUCTION TO FÖRSTER RESONANCE ENERGY TRANSFER

To study the impact of lanthanide doped nanoparticles (LnNP) size, design and morphology onto the effectiveness of FRET, we have conducted simulations relying on the Förster Resonant Energy Transfer (FRET) mechanism[1] and model. Briefly, due to non-radiative and resonant energy transfer between donor (D) and acceptor (A) molecules in relation to distance between them (r_{DA}) and parameters such as Förster distance R_0, the D's luminescence lifetime τ_D is reduced in the proximity of A molecules to τ_{DA}. Simultaneously, the efficiency of resonant energy transfer η depends on the distance following simple Förster relations

$$\eta_{FRET} = \frac{1}{1+\left(\frac{r_{DA}}{R_0}\right)^6} = 1 - \frac{\tau_{DA}}{\tau_D} = 1 - \frac{I_{DA}}{I_D} \qquad \text{Eq. S1}$$

where R_0 is the Förster distance, which is the D-A distance, at which the efficiency of resonance energy transfer is 50% of the maximum.

The very steep (6th power) distance dependency of RET efficiency between D and A species (Eq. S1), originates from dipole-dipole interactions, while the more relaxed (2nd power) distance dependence for radiative energy transfer is a result of reabsorption probability of D emitted photons by A centers. The efficiency of the radiative energy transfer is also dependent on geometry of the container, and concentration and optical properties of the acceptor. Moreover, in radiative energy transfer the luminescence lifetime of D does not change with the presence of A (in such case $\tau_{DA} = \tau_D$) and also the observed induced A emission follows the decay of D (here also $\tau_{AD} = \tau_D$) independent on the r_{DA} distance.

Beside the condition of RET on significant spectral overlap between D emission and A absorption cross section, the D and A species must stay in close proximity to allow non-radiative transfer of the excited-state energy from D to A. Because in the case of LnNPs, the RET phenomenon occurs in a configuration of individual nanoparticles doped with significant number of D_i ions and numerous A_j molecules can be attached to the surface of such donor particle, the ensembles of D and A species in a given configuration are denoted as $\langle D \rangle$ (a set of D_i within single NP) and $\langle A \rangle$ (a set of all A at possible surface

sites), respectively. The r_{DiAj} indicates the distance between the individual donor (D_i) and the closest acceptor molecule (A_j).

In the first approximation, when considering lanthanide doped UCNPs as a RET donor, one finds at least two different classes of activators as D species, the "core" and "superficial" ones. Actually, there is a smooth transition between one role and the other, depending on the actual distance (r_{DiAj}) between the given D_i of the NPs and the closest acceptor A_j. Obviously, the relative amount of the latter to the former will influence the suitability of such NPs as donors for RET mechanism. The energy will be transferred through RET efficiently only if D_i stays closely enough to A_j ($r_{DiAj} < R_0$) and otherwise the efficiency drops rapidly. This means the ions in the core (D_i) contribute to the emission of the whole NPs, but are not directly susceptible to RET and can only contribute radiatively to the presence of acceptor molecules, thus $\tau_{DA} = \tau_D$. The D_i in proximity to the NP surface and surface-bound A_j molecules, however, are potentially susceptible to RET or quenching through surface and thus $\tau_{DA} < \tau_D$. These "superficial" ions can, however, also contribute to radiative energy transfer, but opposite to non-radiative resonant energy transfer, the efficiency of the radiative ET (even at short distances), is strongly limited by the concentration of acceptor molecules. The photons emitted by the D are randomly directed in space, and the subsequent reabsorption of D photon by A requires that either the A molecules are present at high enough concentration or the geometry of the container provides extended path lengths for the emitted photos to result in all significant absorption at emission wavelength of the donor. The radiative ET can thus occur at much larger distances, but on the other hand, it is on the whole significantly less efficient than RET and does not respond so specifically to surface bound A_j molecules. In general the radiative ET display significant contribution to the observed signal of sensitized emission only when there is high excess of D species that cannot participate to RET and in case the A concentration is high enough to result in significant overall absorption of photons emitted by the D. Thus, in practice, the radiative ET is relevant only in circumstances where the total A concentration is at least at micro molar range (with high enough epsilon) resulting in absorption of several percent of the D emission. This absorption depends also on possible path lengths and volume dimensions around the donors.

Recasting the equation S1 allows expressing the luminescence lifetime of D paired with A as a function of relative distance between the two species.

$$\tau_{D_iA_j}(r) = \frac{\tau_D}{1 + \left(R_0/r_{D_iA_j}\right)^6} \qquad \text{Eq. S2}$$

One may therefore easily examine all of the D ions present in the NP volume, by iterative calculating the distance between the given D_i ion and the nearest A_j molecule located at the surface (Fig. S3i-iii). Different UCNP architectures simulated by virtual nanoparticle (VNP) model are presented in Fig. S3iv (a - f): (a) small, (b) medium size and (c) large core only (homogeneously doped) UCNPs (VNP:20Yb2Er), (d) active-core-undoped-shell (VNP:20Yb2Er@...), (e) sensitized-core-active-shell with 2% Er^{3+} (VNP:20Yb@20Yb2Er) and (f) with 5% Er^{3+} co-doping in the shell (VNP:20Yb@20Yb5Er). Every single D_i ion has been individually probed by calculating the distance r_{DiAj} to the nearest A_j molecule. Based on these calculations for all available donors, histograms of shortest D-A distances for each D_i denoted as $N(r_{DiAj})$ could be calculated, as exemplary presented in Fig. S3v. Next, $H_r(r_{DA})$ histograms were re-casted to $\tau_{DA}(r_{DiAj})$ according to Eq. 1 to get luminescence lifetime histograms (Fig. S3vi). Finally, by combining the obtained $H_\tau(\tau_{DA})$ histograms with Eq. 2, one may simulate the expected shapes of the acceptor surface coverage dependent donor NP luminescence decays as presented on Fig. S3vii and RET efficiencies based on integrated luminescence kinetics as presented in Fig. S3viii. The expected $H_r(r_{DA})$ and $H_\tau(\tau_{DA})$ and the luminescence decays for different NP designs presented in Fig. S3iv (a – f) are shown on Fig. 2a, Fig. 2b and Fig 2c, respectively. Expected efficiency of RET, i.e. the acceptor dose response on the integrated luminescence kinetics, is presented in Fig. 2d.

1.2 CALCULATION OF FÖRSTER DISTANCE

Förster distance (R_0) is distance between pair of D - A at which the efficiency of energy transfer is equal 50% of the maximum. [1]

$$R_0^6 = \frac{9 \cdot ln10 \cdot \phi \cdot \kappa^2 \cdot J}{128\pi^5 \cdot n^4 \cdot N_A} \quad \text{Eq. S3}$$

Where N_A is Avogadro constant ($6.022 \times 10^{23}\ mol^{-1}$), κ^2 is the dipole orientation factor, ϕ is the photoluminescence quantum yield (QY) of the donor, n is refractive index of the medium and J is the spectral overlap integral (defined in equation S6).

The error for Förster distance was obtained based on equation

$$\Delta R_0 = \sqrt{\left(\frac{\partial R_0}{\partial \kappa^2}\right)^2 (\Delta\kappa^2)^2 + \left(\frac{\partial R_0}{\partial \Phi_D}\right)^2 (\Delta\Phi_D)^2 + \left(\frac{\partial R_0}{\partial N_A}\right)^2 (\Delta N_A)^2 + \left(\frac{\partial R_0}{\partial n}\right)^2 (\Delta n)^2 + \left(\frac{\partial R_0}{\partial J}\right)^2 (\Delta J)^2} \quad \text{Eq. S4}$$

We calculated the error for Förster distance using the partial derivates and based on Eq. S4 we obtain equation from which we indicate error of Förster distance value:

$$\Delta R_0 = \frac{1}{6} \cdot \sqrt{\left(\left((\kappa^2)^{-\frac{5}{6}}\right)^2 \cdot (\Delta\kappa^2)^2 + \left(\Phi_D^{-\frac{5}{6}}\right)^2 \cdot (\Delta\Phi_D)^2 + \left(\frac{-4}{n^{-5}}\right)^2 \cdot (\Delta n)^2 + \left(J^{-\frac{5}{6}}\right)^2 \cdot (\Delta J)^2\right)} \quad \text{Eq. S5}$$

In case of UCNPs the ϕ of the donor used to calculate the Förster distance (R_0) is the internal/intrinsic QY of the donating emissive energy level of the activator, i.e. the rate of radiative relaxations divided by the sum of both radiative and nonradiative relaxations of the selected excited energy level of the activator ion (or calculated from observed lifetime of the emission of directly excited donor divided by maximal radiative lifetime of the selected excited energy level of the donor without any nonradiative relaxation) equal to the probability of the activator ion to emit photon once the ion is excited (independent how it was excited). The total, overall upconversion QY is product of sensitization efficiency and internal QY of the donating emissive energy level of the activator - and in UC we really have a complex sensitization pathway, whose efficiency is excitation power dependent. The effect of the sensitization and the internal QY of the emitting lanthanide ion on the overall QY is discussed in numerous literature examples (such as basis of lanthanides spectroscopy,[2] interactions between lanthanides ions,[3] transfer between Er^{3+} ions in UCNPs and QD [4] and FRET between UCNPs and QDs [5]).

The spectral overlap *J* was calculated with the following relation [1]

$$J = \frac{\int f_D(\lambda) \cdot \varepsilon_A(\lambda) \cdot \lambda^4 d\lambda}{\int f_D(\lambda) d\lambda} \quad \text{Eq. S6}$$

Where $f_D(\lambda)$ is a spectral profile of the D emission, ε_A is the molar extinction coefficient of the acceptor. The κ^2, J, n are the factors, which indirectly affects the FRET efficiency, but their values are either constant ($\kappa^2 = 0.67$ and $n = 1.45$) or defined by the selection of appropriate D and A, which maximize R_0, by selection of highest J (overlap integral between normalized D donor mission and molar extinction coefficient of A). For certain D and A pair the Förster distance could thus be modulated by changing internal QY of the D which is a serious research challenge. This is because

overall upconversion QY is strongly reduced (down to below 0.01%) for UCNPs exposed to aqueous environment and shown to rise only upon passivation with thick shells (L_S = 3 – 10 nm) [6], which however results in increase of the smallest r_{DiAj} distance between D_i and A_j to at least $r_{DiAj} > L_S$. The internal QY of Er^{3+} most likely is also improved due to decreased quenching when the Er^{3+} are more distant from surface or there is passive shell. Therefore, for effective FRET biosensing, not only the chemical architecture has to be optimized (by increasing the surface to volume D ratio), but the gains from increased internal QY of volumetric D ions has to be taken into account.

During calculations of spectral overlap, we normalized the emission spectrum of $NaYF_4$: Er,Yb UCNPs at of wavelength range 475 – 600 nm comprising the emission bands from the $^2H_{11/2}$ and $^4S_{3/2}$ energy levels. Error of spectral overlap can be described with equation:

$$\Delta J = \sqrt{\left(\frac{\bar{I}_D^2(\lambda)}{2}\right)^2 \left(\Delta \bar{I}_D(\lambda)\right)^2 + \left(\frac{\varepsilon_A^2(\lambda)}{2}\right)^2 \left(\Delta \varepsilon_A(\lambda)\right)^2 + \left(\frac{\lambda^5}{5}\right)^2 (\Delta\lambda)^2} \qquad \text{Eq. S7}$$

The overall upconversion QY affects the D intensity and thus also the measured signals – which is also important – yet it does not necessarily change the RET efficiency in case the differences are due to photoexcitation power and sensitization efficiency through Yb^{3+} and not due to internal QY of the donating emissive energy level of the Er^{3+} activator.

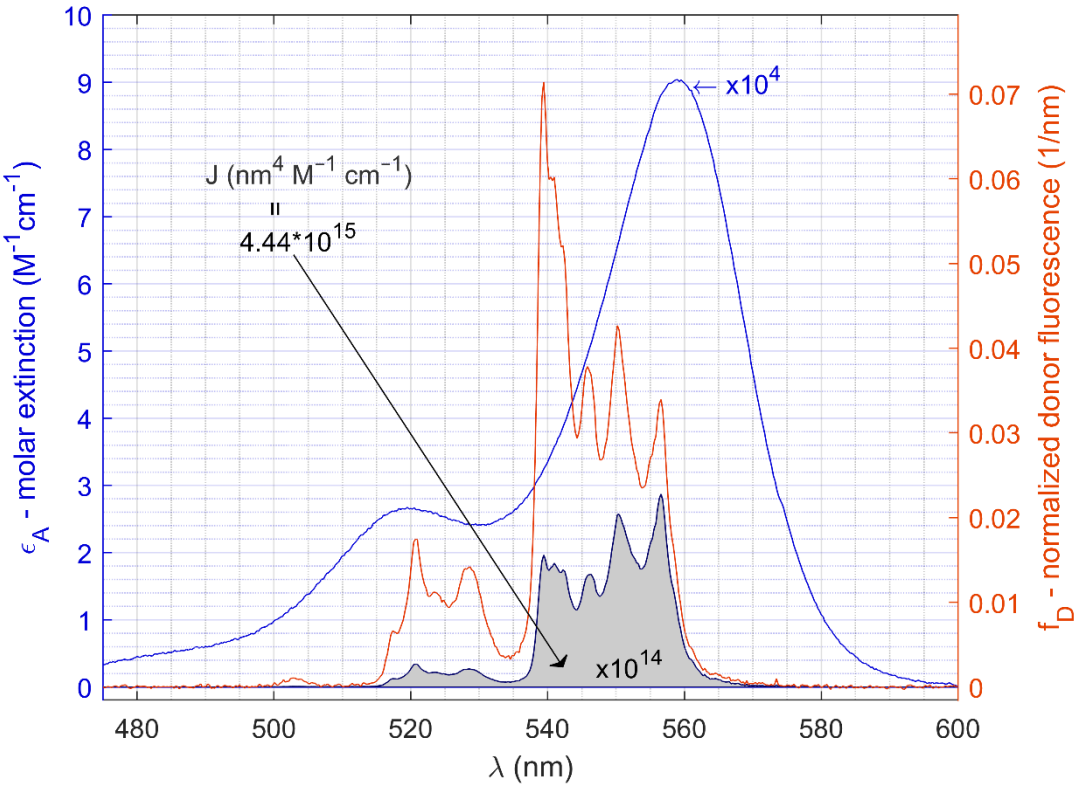

Fig. S1 Spectral overlap graph. Molar extinction of the acceptor ε_A ($M^{-1}cm^{-1}$) (left axis) and normalized donor Fluorescence f_D (right axis). Spectral overlap $J = \varepsilon_A \cdot f_D \cdot \lambda^4$. Extinction coefficient of Rose Bengal dye were taken from. [7]

The internal QY used for calculation of the Förster distance is likely to be much larger than the overall UC-QY, since the UC sensitization process is weak. Also the internal QY of the donating energy level donor could be independent of the excitation intensity (unlike overall UC-QY) and the internal QY could

actually be close to the maximal UC-QY available at high excitation intensity. In our virtual nanoparticle model (VNP) we assume the internal QY of the donating emissive energy level of Er^{3+} donor yet to a conservative value of 0.1% ($\phi = 0.0010$), which is reported for $NaYF_4$:2%Er^{3+},20%Yb^{3+} diameter (no-shell) 30 nm hexagonal NPs. [8,9] The internal QY, however, has a significant impact on the Förster distance (R_0) as shown in Fig. S2d and, thus, also to the distance range where the RET is efficient enough to be applicable as illustrated in Fig S2a. In consequence, the Förster distance could actually be larger than estimated and used in the VNP model, but the used internal QY value is anyway reasonable and not critical to the general conclusions drawn from the VNP model – although the distance range and fraction of donor ions capable of RET would be extended accordingly.

For the refractive index of the medium we used in the VNP model calculations an average value of $NaYF_4$ ($n = 1.48$) [10,11] host matrix and water ($n = 1.333$). The individual Er^{3+} donor ions are embedded in the matrix (at variable depth, but also superficially being exposed directly to the environment), and the acceptor molecules are attached (without any additional ligands) to the surface of the NPs. Thus, the D-A interaction occurs mainly through the space 'filled' with $NaYF_4$ crystalline matrix, but nevertheless, the Rose Bengal (RB) acceptor is still surrounded by water, with its dielectric properties (quantified by its index of refraction) justifying the use of the average value of refractive indexes of $NaYF_4$ and water. The effect of changes in the refractive index on the Förster radius (R_0) is shown in Fig. S2d.

In calculation of R_0 the orientation of the D and A dipole moments is quantified by the orientation factor κ^2. The dynamic averaging makes $\kappa^2 = 2/3$ for freely rotating D and A molecules, such as assuming random and isotropic orientation of the dipoles during the excited state of both D and A. The isotropic orientation, however, is not entirely valid for UCNPs, as the numerous Er^{3+} donor ions have individually rather single orientation direction of their dipole moments in the host matrix, and when the RB acceptor molecules are coordinated directly on the surface, they likely show some preferred orientation at each location. On the other hand, the acceptors can yet randomly anchor on the NP surface at multiple locations, which differ in their preferred orientation on. Further, the lifetime of donating energy level of the Er^{3+} is in the range of micro- up to milliseconds (as compared to nanosecond lifetimes of the acceptor organic molecule), which is enough for the acceptor molecule to likely reorient multiple times before the RET occurs and, thus, the use of dynamic averaging approach seems a reasonable approximation. The orientation factor does not impact severely the calculated R_0 absolute value as illustrated in Fig. S2c. In this context, we have used $\kappa^2 = 2/3$ associated with isotropic orientation also in the VNP model, because our simulations and studies don't aim at quantitative D-A distance determination in absolute terms, and we think the individual κ^2 estimation for every single D_i-A_j pair would unnecessarily complicate the simulation with no real added value for sake of comparison between different architectures.

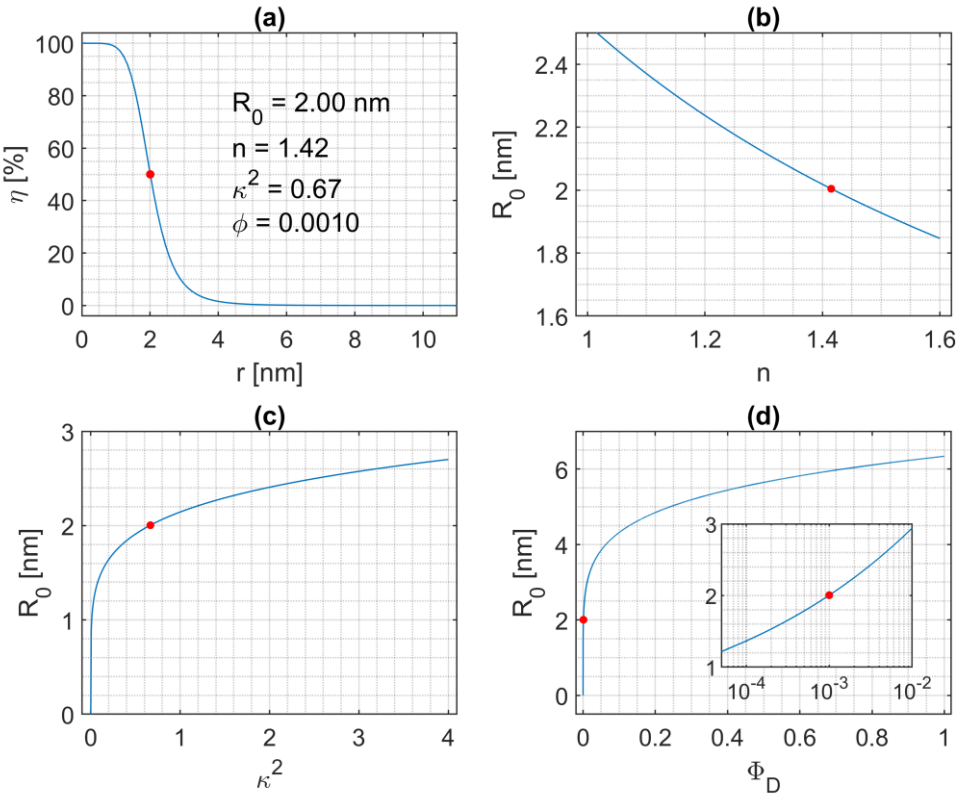

Fig. S2 RET parameters used for VNP modelling. Efficiency of RET in dependence of distance between the donor and the acceptor with fixed parameters used in further calculations (a). The effect of the changes in fixed parameters of the refractive index ($\boldsymbol{n}$) (b), orientation factor ($\boldsymbol{\kappa^2}$) (c), and quantum efficiency of donor ($\boldsymbol{\Phi_D}$) (d) on the Förster distance ($\boldsymbol{R_0}$).

Table S1 Parameters for Förster distance R_0 calculations.

		Value	error	Name of parameter
k^2	-	$\frac{2}{3}$	0.0001	orientation factor
ϕ_D	-	0.001	0.0001	quantum efficiency
N_A	$[mol^{-1}]$	$6.022 \cdot 10^{23}$	-	Avogadro number
n	-	$\frac{1.48 + 1.35}{2}$	0.020	refractive index
J	$[nm^4 M^{-1} cm^{-1}]$	$4.44 \cdot 10^{15}$	$8.97 \cdot 10^{10}$	spectral overlap
λ	$[nm]$	$475 - 600$	0.01	Wavelength range
ε_A	$[M^{-1} cm^{-1}]$	See graph above, Fig S1	12	Molar extinction of acceptor
f_D	$[1/nm]$	See graph above, Fig S1	-	Normalized emission of donor

The spectral overlap of $J = 4.444 \cdot 10^{15} \pm 0.0001 \cdot 10^{12}$ was obtained calculated according to Eq. S6 and S7 using the spectral data illustrated in the Fig. S1 for the $NaYF_4$: Yb, Er donor and Rose Bengal acceptor. Förster distance $R_0 = 2.00 \pm 0.24$ was calculated based on Eq. S3 and Eq. S5 using the obtained value of spectral overlap and assumed values for the refractive index (n), orientation factor (κ^2) quantum efficiency of donor (Φ_D) discussed above and summarized in Table S1.

$$R_0 = \left(\frac{9 \cdot \ln(10) \cdot (2/3) \cdot 0.001}{128 \cdot \pi^5 \cdot 1.415^4 \cdot 6.022 \cdot 10^{23}} \cdot (4.44 \cdot 10^{15} \cdot 10^{17})\right)^{\frac{1}{6}} = 2.001 \pm 0.24\ [nm] \qquad \text{Eq. S8}$$

MATHEMATICAL MODELLING OF UPCONVERSION RET

Virtual nanoparticle (VNP) model allows to obtain distribution of dopant ions (such as Yb^{3+} and Er^{3+} ions) in crystal lattice and is a promising tool for theoretical and experimental research on the impact of compositional architecture of UCNPs. Calculation of the simulated net effect of FRET between Er^{3+} dopant ions (donor) in the NP and Rose Bengal (RB) organic dyes (acceptor) coordinated on the NP surface was based on the parameters defined in Table S1 and locations and distances of individual donor ions and bound acceptors obtained from the VNP model. Starting from the crystallographic structure of β–$NaYF_4$ taken from crystallographic database ICDD 04-011-3581 (Fig. S6, Fig. S3i) and definition of core diameter and shells thickness (Table S2, Fig S3ii), a 3D spherical core-shell VNP was designed (Fig. S3iii) by replicating respective number of unit cells in X,Y and Z directions. Next, a fixed donor ion number have been evenly distributed either in the core or the shell. Acceptor sphere at the surface of nanoparticle were created based on sphere equation, with defined density of positions for dye.

Further analysis of the VNPs and their luminescent properties (schematically calculations for spectral overlapping shown in Fig. S1) were studied using Förster formalism. Based on D and A distribution (D_i and A_j, respectively) within VNP, the 3D position coordinates served to calculate the shortest distance between every single D_i and its closest neighbor A_j. Such distribution was shown as a histogram of D-A distances $H_r = H(r_{DA})$ (Fig. 2a) overlapped with calculated Förster efficiency curve. We assumed τ_D to be equal 120 μs, and R_0 was fixed to 2.00 ± 0.24 nm, as calculated for Er^{3+} donors and Rose Bengal acceptor. Based on these D-A distance histograms, the r_{DA} distance has been converted to expected D lifetime τ_{DA} (which means D lifetime in the presence of A) according for Eq. 1 (Fig. 2b) to generate $H_\tau = H(\tau_{DA})$ histograms of luminescent lifetimes of individual D ions. Next, luminescence intensity kinetics were calculated (Fig. 2c) by summing up the H_τ, being the contribution of all available D ions, based on the Eq. 2. Finally, this procedure was repeated for 0.1% to 100% coverage of VNP surface with acceptor (i.e. concentration of A) and the RET efficiencies were calculated from the integrated luminescence kinetics (Fig. 2d) for individual VNPs using the Eq. 3.

The acceptor surface coverage (A concentration) dependence (Fig. 2) is colour coded, thus black to red colour on Fig. 2 is corresponding to each other between all for $H_r([A])$, $H_\tau([A])$, $I(t,[A])$ and $\eta_{FRET}([A])$. Because the number of D ions within all the studied VNPs do not go beyond a few hundreds, all these calculations were repeated 3 times and averaged for three, repeatedly 'synthesized' VNPs.

1.3 THE VIRTUAL NANOPARTICLES

For the evaluation of different core-shell architectures six different VNPs were designed and evaluated: The VNP models generated were: (i) small core s_YbEr, (ii) medium core m_YbEr, (iii) Large core l_YbEr, (iv) active core @undoped shell, Yb,Er@..., (v) sensitized core @ active shell with 2% Er, Yb@Yb,Er and

(vi) with 5% Er in the shell, Yb@Yb_5Er. The tables of structural composition (Table S2), characteristics of the morphology (Table S3) and statistics of the dopants (Table S4) enumerate the basic properties of the VNPs models.

For each VNP model, we define dopant concentration and diameter of nanocrystal in the Table S2. Based on this input data, we calculated volumes (V) and surfaces (S) for each nanoparticle as well as the ratios between V and S presented in the Table S3. V and S define also the number of activator ions available (as donor) for RET and the maximal number of organic dyes (as acceptor), which can be attached to the surface of NPs.

Table S2 Parameters for generation of function of VNP structures.

	Core radius	Dopant concentration		Shell thickness	Dopant concentration		NP diameter
		Yb^{3+}	Er^{3+}		Yb^{3+}	Er^{3+}	
Structure	nm	%	%	nm	%	%	nm
s_YbEr	4	20	2	0	-	-	8
m_YbEr	8	20	2	0	-	-	16
l_YbEr	12	20	2	0	-	-	24
Yb,Er@...	12	20	2	2	0	0	28
Yb@Yb,Er	12	20	0	2	20	2	28
Yb@Yb_5Er	12	20	0	2	20	5	28

Table S3 Parameters of VNPs: diameters, volume, surface, ratio volume to surface, surface to volume.

	Shell thickness	Core diameter	NP diameter	Volume			Surface	S/V	V/S
				core	shell	NPs			
Structure	nm	nm	nm	nm^3	nm^3	nm^3	nm^2		
s_YbEr	0	8	8	268	0	268	201	0.75	1.33
m_YbEr	0	16	16	2145	0	2145	804	0.38	2.67
l_YbEr	0	24	24	7238	0	7238	1810	0.25	4.00
Yb,Er@...	2	24	28	7238	4256	11494	2463	0.21	4.67
Yb@Yb,Er	2	24	28	7238	4256	11494	2463	0.21	4.67
Yb@Yb_5Er	2	24	28	7238	4256	11494	2463	0.21	4.67

Table S4 Data of statistics from VNP model related to donor ions and acceptor molecules coverage.

Er^{3+} ions concentration	Er^{3+} ions number	Max no. of RB molecules

Structure	%	Counts	counts
s_YbEr	2%	169	25
m_YbEr	2%	1348	121
l_YbEr	2%	4550	256
Yb,Er@...	2% in core	4554	441
Yb@Yb,Er	2% in shell	4329	441
Yb@Yb_5Er	5% in shell	10821	441

RET simulations performed with VNPs require knowledge of maximal surface density of RB molecules which can be adsorbed on the surface of each VNP. We estimated the maximal RB numbers on UCNPs based on the surface area per RB dye obtained from the data by Muhr et. al., [12] by calculating the surface area per dye according to Eq. S9 from the experimental results determined as a combination of absorbance and luminescence spectroscopy for NPs of different diameter. The median for all NPs from 10.1 nm to 42.8 nm in diameter was 22.97 nm^2 per RB and the maximal surface density with only 7.8 nm^2 surface area per RB was obtained with NPs 34.1 nm in diameter.

$$A_{RB} = \frac{4\pi\,(R_{NP})^2}{N_{RB}} \qquad \text{Eq. S9}$$

Based on the information of the minimal surface area per RB and the calculated surfaces of the VNPs (Table S3) we calculated maximal RB numbers for each of the VNPs (Table S4). To simulate RB concentration dependent properties, we found for each VNP the randomly distributed surface nodes (defined by radial coordinates θ and φ), where individual RB molecules which may be anchored on the surface. The 100% acceptor surface coverage (the highest acceptor concentration) means that all the maximal number of RB molecules is present and all the nodes are occupied. To simulate the lower RB concentrations the number of occupied nodes is scaled down proportionally to the surface coverage percentage and the occupied nodes are randomly distributed among the surface nodes.

1.4 VIRTUAL NANOPARTICLE MODEL

First, histograms (Fig. S3v; $H_r(r_{DA})$) of closest D_i-A_j distances (r_{DA}) were calculated which were then re-casted to luminescence lifetime histograms (Fig. S3vi; $H_\tau(\tau_{DA})$

Next, the cumulated luminescence intensity decay (Fig.S3vii) of the $^4S_{3/2}$ energy level of Er^{3+} in the whole VNP was calculated over all available $\boldsymbol{D_i}$ ions:

$$I_{DA}(t,[A]) = \sum_{\mathrm{i}} \mathrm{H}_\tau(\tau_{\mathrm{D_iA}}) \cdot \exp\left(\frac{-t}{\tau_{\mathrm{D_iA}}(r_{DA})}\right) \qquad \text{Eq. S10}$$

Finally, RET efficiencies at different acceptor surface coverages for all simulated VNPs (Fig. 3viii) were evaluated based on integrated luminescence kinetics (Fig. S5), using a formula:

$$\eta_{RET} = 1 - \frac{\int I_{DA}\,(t,[A])}{\int I_D\,(t)} \qquad \text{Eq. S11}$$

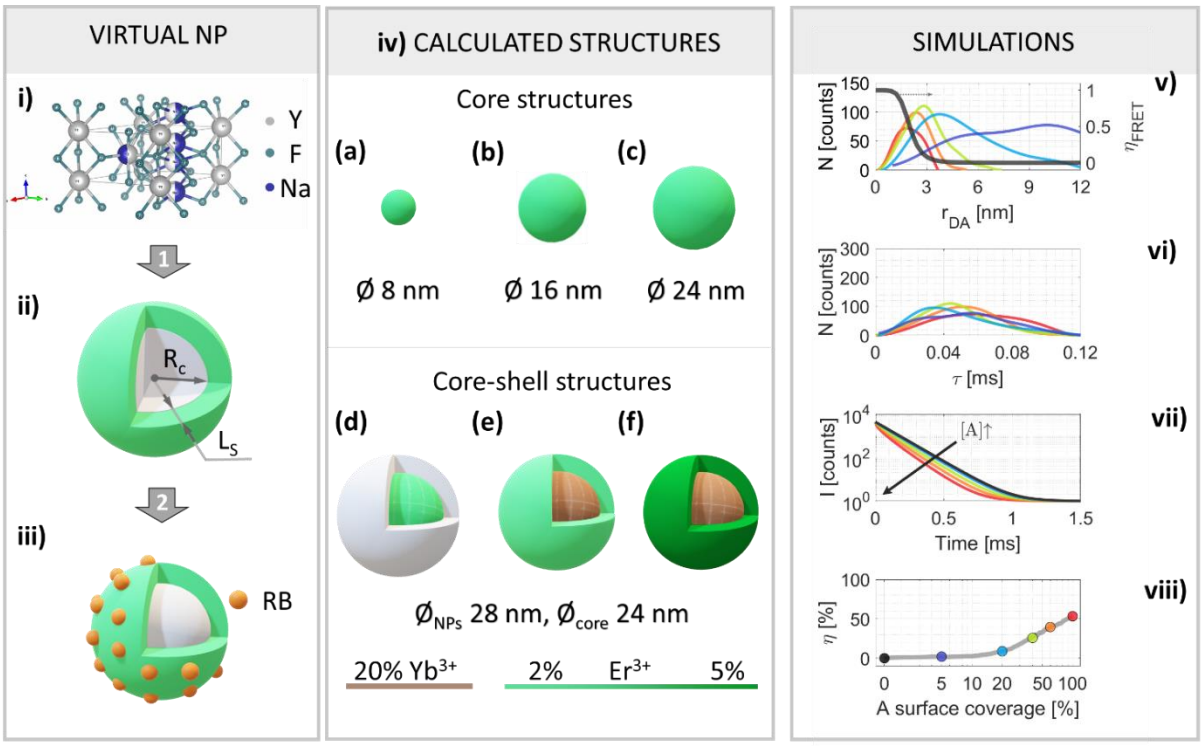

Fig. S3 Schematic explanation of RET simulation with VNPs as donors and different surface coverages of acceptor molecules. The VNPs were designed using (i) crystallographic structure of β-$NaYF_4$, concentration of sensitizer (Yb^{3+}) and activator (Er^{3+}), (ii) core radius (R_C) and shell thickness (L_S), (iii) different surface coverages (acceptor concentrations) with Rose Bengal acceptor; (iv) various VNPs structures were simulated such as (a) small, (b) medium size and (c) large core only UCNPs (VNP:20Yb2Er), (d) active-core-undoped-shell (VNP:20Yb2Er@...), (e) sensitized-core-active-shell with 2% Er^{3+} (VNP:20Yb@20Yb2Er) and (f) with 5% Er^{3+} co-doping in the shell (VNP:20Yb@20Yb5Er), respectively. Colours shown in tested architectures indicated dopant concentration: light and dark green as 2% and 5% of Er^{3+}, grey as undoped with Ln^{3+} ions, brown colour as Yb^{3+} dopant. Such VNP models enabled to calculate acceptor concentration (i.e. surface coverage) dependent: (v) the histograms $H_r(r_{DA})$ of donor-acceptor distances r_{DA}, (vi) luminescence lifetime histograms $H_\tau(r_{DA})$, (vii) corresponding expected luminescence decays of donor nanoparticles and finally the (viii) RET efficiency (η). The colours of the histogram lines on panels (v : D-A distance) and (vii): simulated luminescence decays) correspond to relative acceptor concentration (corresponding points on panel (viii)) - 100%-red ●, 60%-orange ●, 40%-green ●, 20% blue ●, 10% - violet ●, 0% - black ●.

1.5 INTERPRETATION OF HISTOGRAMS

The H_r histograms are simple to interpret, as these are histograms of distances between every single D_i to the nearest acceptor A_j molecules. In our calculations, for sake of simplicity, we assumed the RET occur between nearest neighbours, because RET between such pair is the most efficient. The VNP model thus takes into account only direct RET from each of the excited donors and excludes the possibility of post-excitation energy migration and re-charging of the superficial donors. Moreover, since the luminescence lifetime of RB acceptor is very short (nanosecond time scale) compared to long luminescence lifetime of the donor ions (around 120 μs, preceded short risetime), we assumed that that single A_j is almost always ready to accept energy from donor and can thus act as acceptor simultaneously from multiple D_i in case it is the closest acceptor to them all.

The interpretation of H_τ are, however, not obvious, because the r_{DA} to τ_{DA} relationship is non-linear and 6th power dependent. This means also that the calculated $I(t)$ luminescence kinetics is not trivial to understand. For this reason, we modelled donor VNPs with full A surface coverage and calculated the expected luminescence lifetimes for a few regions of the H_r histograms (Fig. S4a), each region illustrating the partitive contribution of D_i at certain distance range to A.

The H_r histograms are not homogenous, and for the small homogeneous YbEr and the Yb@YbEr VNPs show the majority of Er^{3+} donor ions (in number around 200 ions for Yb@YbEr) stay at around 2 nm from acceptors (Fig. S4a), which are directly anchored to the surface of VNPs. The H_r histograms are converted to H_τ histograms (Fig. S4b), which then serve to calculate luminescence intensity kinetics according to Eq. 2. Fig. S4c shows contributions from groups of D_i at increasing distance ranges of A to the total donor luminescence kinetics. This demonstrates that the D_i in very close proximity to A are efficiently able to transfer their energy to A and due to efficient RET their luminescence is very short living. Therefore, in time-gated detection the contribution of the most superficial D to the total $I_D(t)$ occurs only rapidly after excitation and can be challenging to measure. In steady-state detection, however, their contribution to the sensitized acceptor emission could actually be enhanced as the shortened luminescence lifetime results in that they are rapidly recharged under continuous excitation.

When the D_i to A distances increase and approach to ~R_0 distance the efficiency of energy transfer drops rapidly and the effect on the luminescence lifetime diminishes and disappears approximately at distances twice the R_0 distance. Then, the luminescence lifetime τ_{DA} is easily measurable, but does not differ anymore from D only luminescence lifetime τ_D. The most important changes in lifetime, which are easy to record and distinguish from D only luminescence lifetime, are observed for D_i staying in range 0.7 to 1.5 × R_0 distance from A. This suggests how the optimal donor NPs for lifetime based sensing should be designed: First, the D ions should be removed from the center of the NPs as was qualitatively proposed earlier. However, partly unexpected conclusion is the fact, the D ions should actually not be too close to A. This can potentially be achieved by passivating the RET NPs with undoped shell, but because the NPs require proper biofunctionalization to enable bispecific recognition, one needs to carefully consider the D_i to A distances available with the NP bioconjugates. In addition to the thickness of the possible undoped shell, the distances will obviously depend on the thickness of surface functionalization, the size of ligands, bio-specific molecules and acceptors.

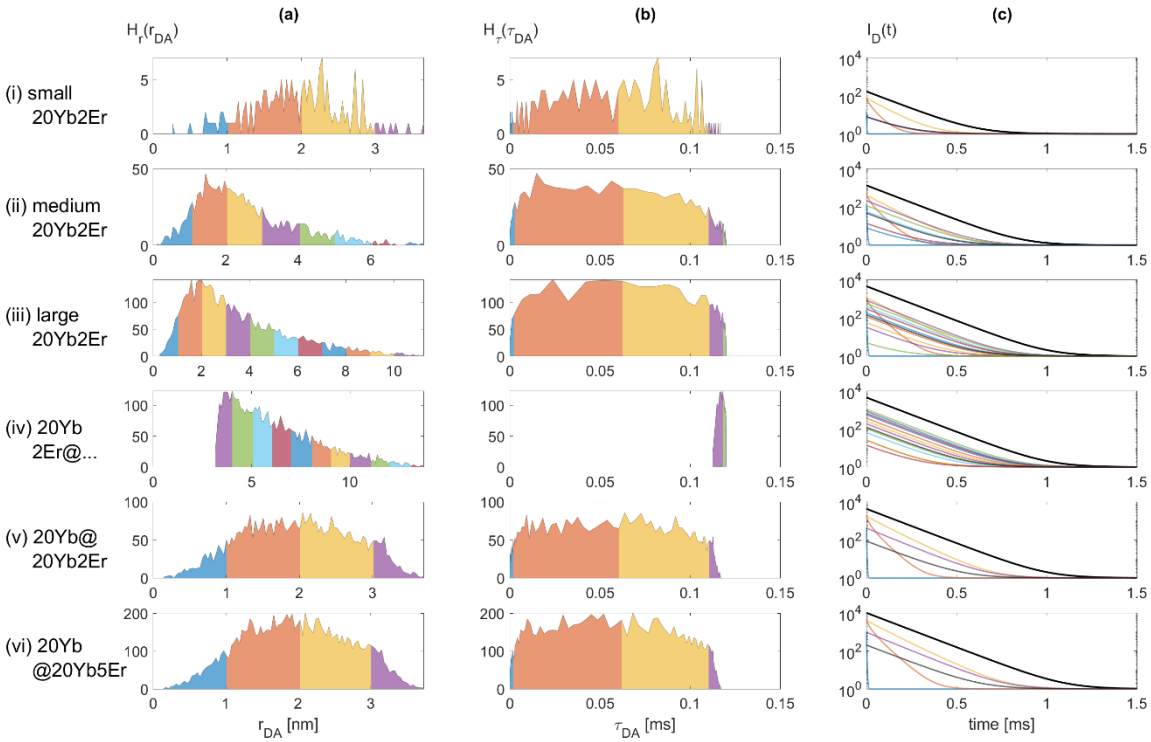

Fig. S4 VNP model RET simulation of partitive contribution of the donor ions with different acceptor distances to the donor luminescence kinetics. Contribution of (a) D_i to A_j distances illustrated in histogram H_r and (b) D_i luminescence lifetimes shown in histogram H_τ to the (c) donor luminescence kinetics for YbEr, YbEr@... and Yb@YbEr VNPs. Each colour represents a group of D_i ions at similar (within 1 nm) distance from acceptor. The black curve in (c) is total D luminescence kinetics with no A present.

The resonance energy-transfer (RET) efficiency for six different modelled VNP architectures with different acceptor surface coverages is presented in Fig. S5. The highest efficiency with full acceptor surface coverage is obtained for core-shell architectures with Er^{3+} ions in shell (20Yb@20Yb2Er, 20Yb@20Yb5Er), but also for small NPs (20%Yb2Er). Interestingly the small 20Yb2Er gives high RET efficiency already with lower acceptor surface coverable, but it has disadvantage of small emission intensity (due to lower number of lanthanides ions and, in practice, also due to stronger surface quenching effects competing with energy-transfer to acceptor).

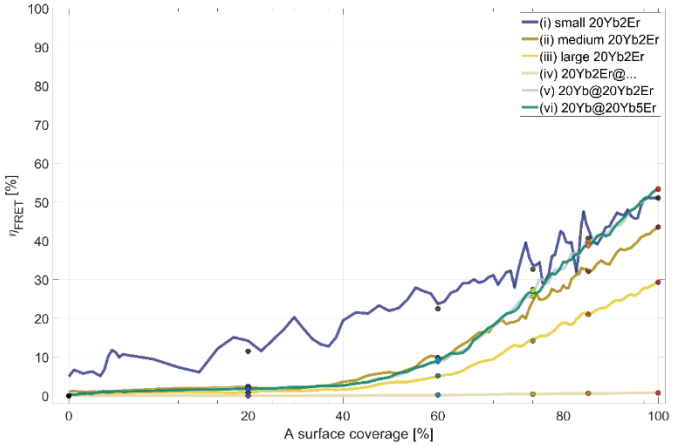

Fig. S5 VNP model RET simulation of the effect of acceptor surface coverages on the RET efficiency calculated by the integrated donor luminescence kinetics. Data is the same as shown in Fig. 2d (i)

small 20Yb2Er as blue ●, (ii) medium 20Yb2Er as dark yellow ●, (iii) large 20Yb2Er as yellow ●, (iv) 20Yb2Er@... as beige ●, (v) 20Yb@20Yb2Er as grey ●, (vi) 20Yb@20Yb5Er as green ●.

2 MATERIALS AND METHODS

2.1 THE STUDIED SAMPLES

In order to experimentally investigate the influence of localization of Yb^{3+} UC sensitizers and Er^{3+} donors on RET sensitivity and efficiency a series of Er^{3+} and Yb^{3+} co-doped β-$NaYF_4$ core-shell materials were prepared, namely …@Er, Yb@Er and Yb@YbEr. In order to further investigate the influence of localization and Er^{3+} concentration a series of additional Er^{3+} and Yb^{3+} co-doped β-$NaYF_4$ core shell materials with different concentration of Er^{3+} in the shell were synthesized with well-defined crystal structures and morphology. More precisely, synthesized six samples were prepared with the same core $NaYF_4$:20%Yb^{3+} and shells including $NaYF_4$:20%Yb^3 with different concentration (0.1%, 0.2%, 0.5%, 3%, 4%, 5%) of Er^{3+} ions.

2.1.1 STRUCTURE AND MORPHOLOGY OF THE UCNP SAMPLES

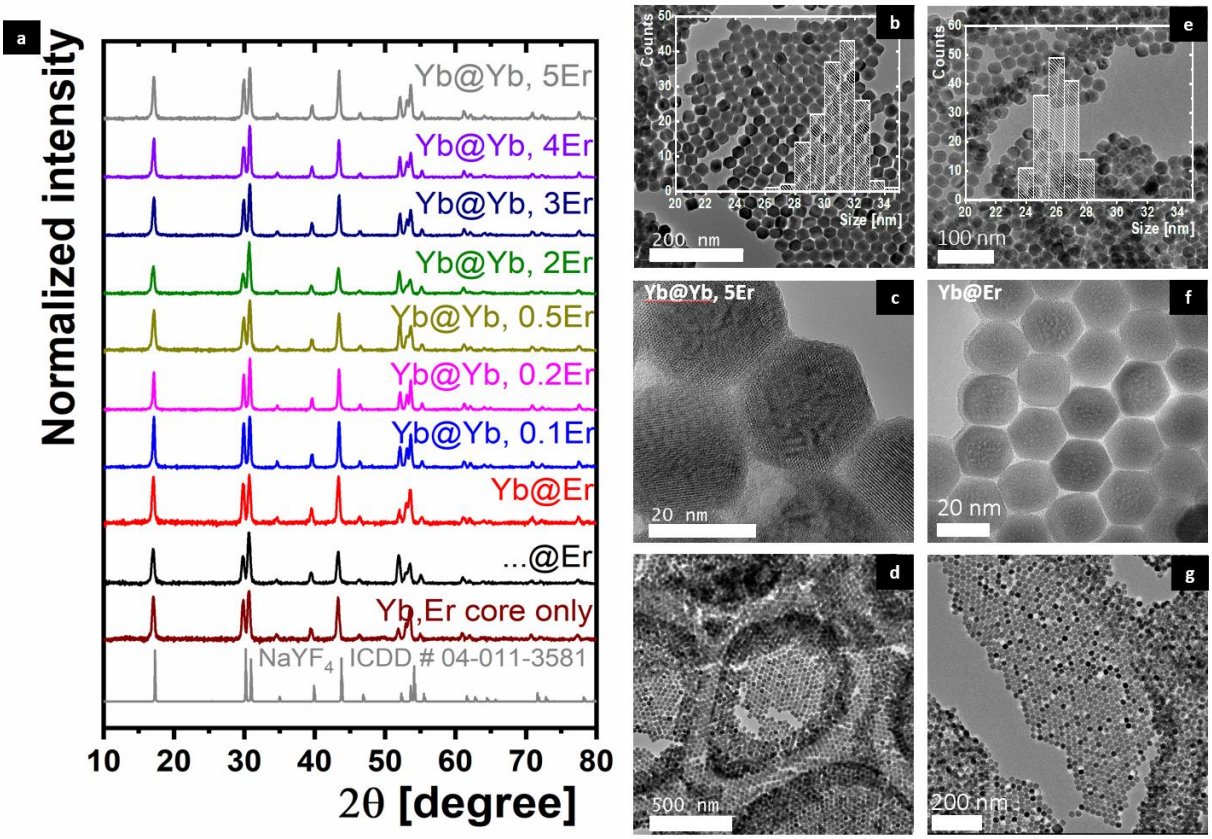

Fig. S6 Structure and morphology of the UCNP samples. (a) The XRD patterns for all prepared samples, and representative TEM images with size histograms for (b) YbEr core only sample, (c,d) Yb@Yb5Er and (e-f) Yb@Er samples.

The structures of the different core-shell UCNP architectures were confirmed by X-ray diffraction (XRD) and transmission electron microscopy (TEM). The XRD patterns of all samples are presented in Fig. S6a.

All reflections belong to the hexagonal structure(space group: P63/m) of $NaYF_4$ (according to reference ICDD no. 04-011-3581). No additional peaks can be found.

Representative TEM images of each architectures of synthesized UCNPs are shown in Fig. S6 b-d. Due to difference only in Er^{3+} concentration in Yb@YbEr architecture only representative sample with 5% of Er^{3+} was chosen and presented. As it is clearly visible that the nanoparticles are spherical in shape and homogenous with the narrow size distribution. The core material is around 24-26 nanometers in size, and core@shell is around 30 nm, so the shell thickness is around 2-2.5 nm.

3 STEADY-STATE AND KINETIC LUMINESCENCE SPECTROSCOPY

3.1 STEADY–STATE RESONANCE ENERGY TRANSFER MEASUREMENT

The experimental study of FRET with the synthesized UCNPs was performed by mixing the oleic acid stripped UCNPs with the Rose Bengal (RB) dye to bind the RB molecules onto the surface of the UCNPs by adsorption and coordination [13]. In upconversion RET experiments upon excitation the Er^{3+} and Yb^{3+} co-doped UCNPs by 980 nm NIR radiation, the sensitised emission of the surface-bound fraction of the RB was observed at wavelength matching the broad-band RB emission around 575 nm and with minimal direct emission of the Er^{3+} donor, i.e. at 570–630 nm. The strongly distance dependent RET-excited sensitized acceptor emission and the significantly less distance-dependent acceptor emission by reabsorption of donor emission, however, have similar spectral response. In order to be able to estimate the contribution of these two processes to the sensitized acceptor emission, a special surface blocking experiment was carried out before mixing the oleic acid stripped UCNPs with the Rose Bengal (RB) dye. The surface of the UCNPs was blocked with coordinated phosphate, which also promoted the negative surface charge and repulsion towards the binding of the negatively charged RB.

The purpose of the blocking experiment was to measure the sensitized acceptor emission intensity in two different cases: 1) the RB dye is mixed with and attached directly onto the surface of the UCNPs, the D_i to A distances are very short and the non-radiative RET mechanism should dominate; 2) the surface of UCNPs is first blocked by phosphate buffer, i.e. the phosphates coordinate and occupy the surface promoting repulsion and leaving no space for surface binding of the RB dye, which is mixed thereafter with UNCPs. The RB dye is present in in the solution surrounding the UCNPs, but not on the surface, resulting in D_i to A distances much larger than the Förster distance, which minimizes the possibility of RET and renders the possibility for the reabsorption based process to be quantified. In our RET experiments, in the case 1) sensitized emission of the RB dye was observed, but in case 2) there was only negligible emission in the RB dye region. Concluding, the sensitized emission of the RB dye observed in the case 1) is strictly distance-dependent and must be obtained by RET from the Er^{3+} donors to the RB molecules. The strict distance dependence of the sensitized emission is the direct evidence of RET occurrence in our samples. The detectable sensitized RB dye emission in case 2) blocking experiments was only observed with the highest RB concentrations which resulted in significant absorption of the Er^{3+} donor emission in volume employed.

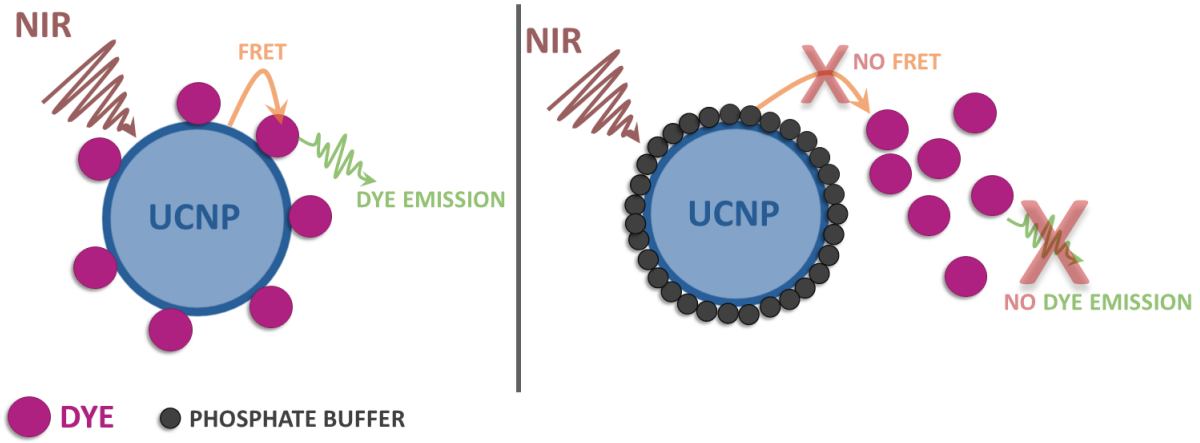

Fig. S7 Scheme of RET experiments to estimate the contribution of the reabsorption process on the sensitized acceptor emission using UCNPs as donor and surface bound Rose Bengal dye as an acceptor. (Left) Without phosphate buffer the acceptors are bound on the donor surface minimizing their distance to facilitate strictly distance-dependent non-radiative energy-transfer process, while (right) in presence of the phosphate buffer the surface is blocked and the donor-acceptor distances are beyond the Förster distance rendering the sensitized acceptor emission only possibly by reabsorption based radiative energy transfer. Representative results of phosphate buffer blocking control experiments are provided on Fig. S10.

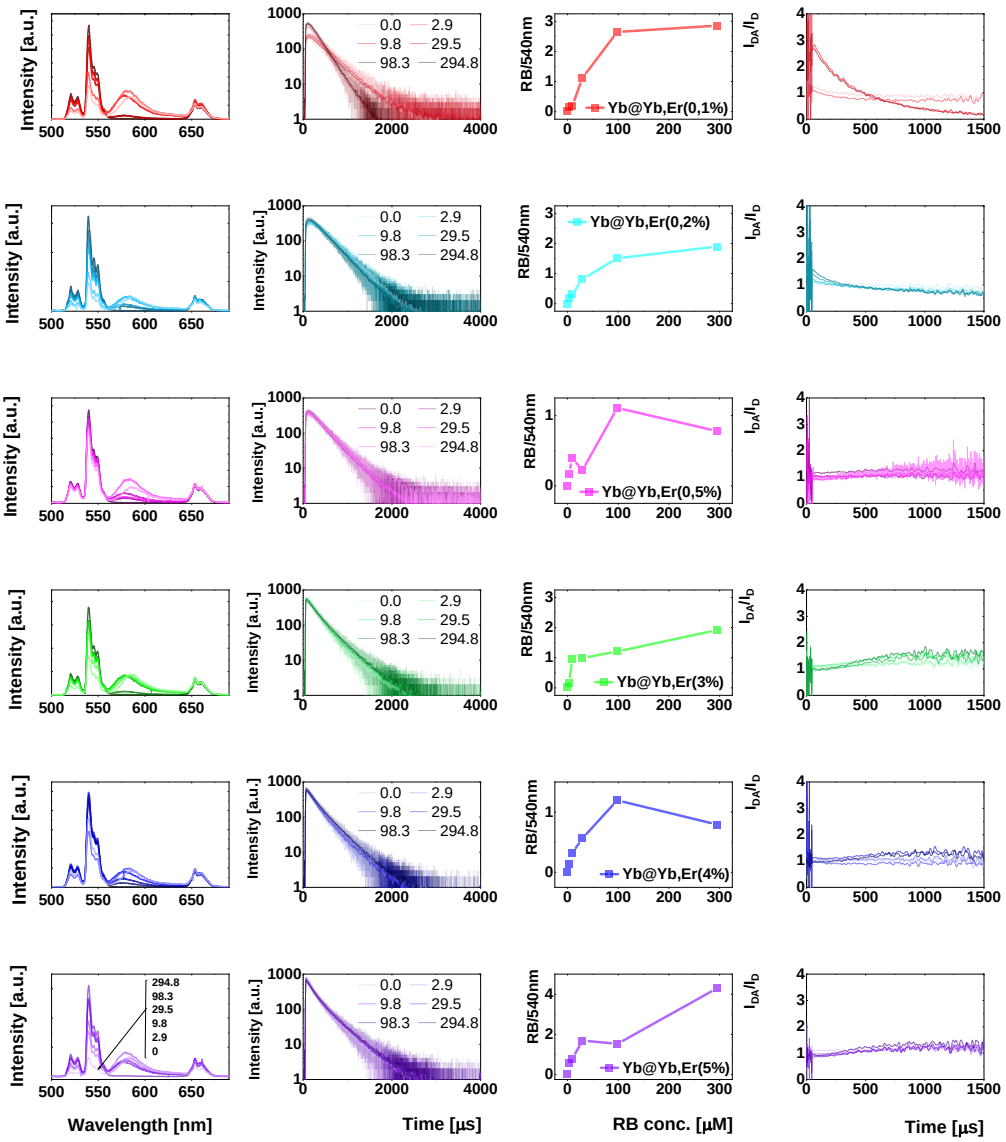

Fig. S8 Steady state and time domain spectroscopy studies of RET sensitized Rose Bengal emission with Yb@YbEr samples with varying Er^{3+} concentration. The upconversion emission spectra (first column), Er^{3+} donor luminescence kinetics (second column) after pulsed excitation (2 µs pulse width), disparity in donor luminescence kinetics (third column) ($\delta_{DA/D} = I_{DA}(t)@550 \,/\, I_D(t)@550$) and ratio of RB emission intensity at 590 nm to Er^{3+} emission at 540 nm (fourth column) measured under 976 nm photoexcitation without the presence of phosphate buffer for Yb@Yb, x%Er (x = 0.1%, 0.2%, 0.5%, 3%, 4%, 5%) samples. The gradient corresponding to the concentration of the dye attached on the surface- from the darkest (0.0 µM of dye) to the brightest (294.8 µM of dye) lines.

Upon increase in the RB dye concentration, one may note the spectral red-shift of the sensitized acceptor emission band in the steady-state spectra of FRET experiments (Fig. S9), which may indicate either the formation of aggregates of RB molecules on the surface of the UCNPs at higher RB content or evidence the inner filter effect[14].

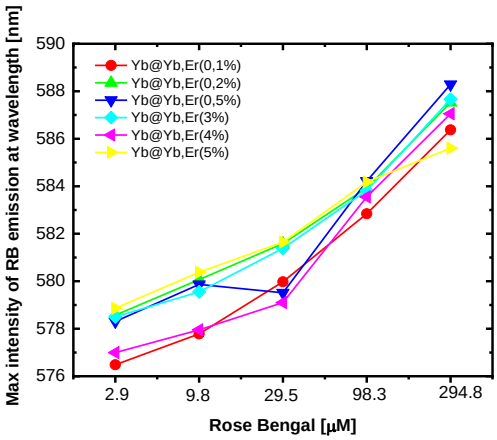

Fig. S9 Wavelength at which the maximum intensity of the RET sensitized Rose Bengal emission occurs. The values plotted for Yb@Yb,Er samples prepared with various concentrations of Er^{3+} were obtained using Lorentz function.

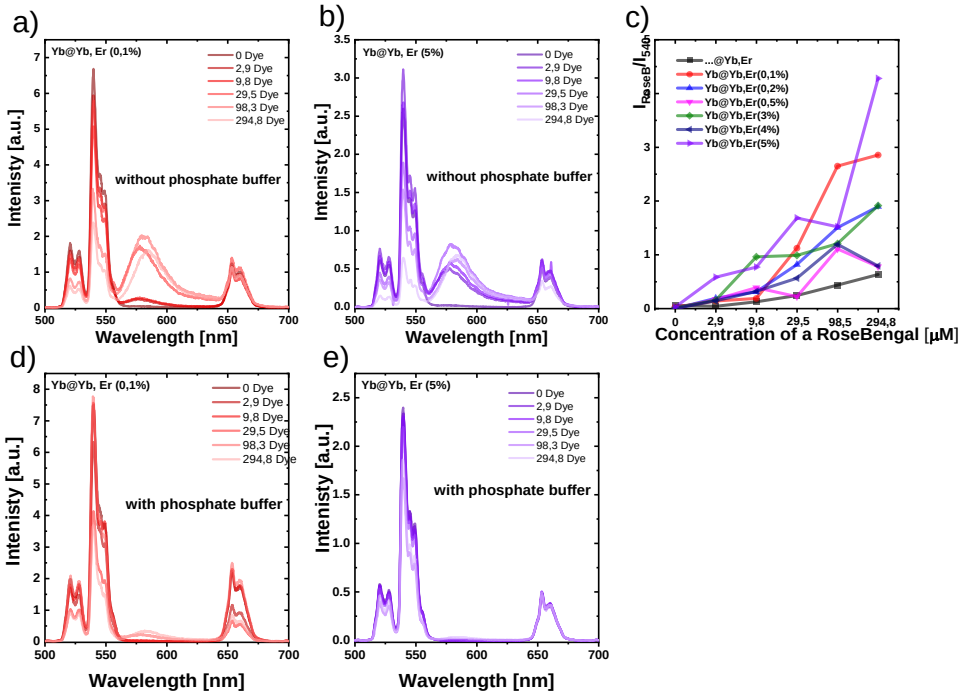

Fig. S10 Representative control experiments demonstrating that phosphate buffer blocks surface ligands and prevent them from binding Rose Bengal acceptor.

3.2 ANALYSIS OF DONOR AND SENSITIZED ACCEPTOR LUMINESCENCE KINETICS

Analysis of decay times with fitting errors are presented in Tables S5 and S6. For the Yb@YbEr sample, the decay kinetics required bi-exponential fit, and thus the amplitude of the short component (A_1) is provided as a percent contribution to the whole fit

$$y(t) = y_0 + a_1 \cdot \exp\left(-\frac{t}{\tau_1}\right) + a_2 \cdot \exp\left(-\frac{t}{\tau_2}\right) \qquad \text{Eq. S12}$$

and the relative contribution of short component is calculated with $A_1 = \frac{a_1}{a_1+a_2} \cdot 100\%$

Table S5 Comparison of decay times and LRET efficiencies for …@Er, Yb@Er and Yb@YbEr UCNPs with RB anchored on their surface. The concentration of a dye was different in every sample and was chosen based on the highest Rose Bengal emission intensity. The bi-exponential decay model was used everywhere, where mono-exponent was not sufficient to fit data reasonably. For bi-exponential decays, the contribution of short component was additionally provided in brackets (A_1 in %)

	Decay time τ_1 [, τ_2] [µs] (A_1 %)						Efficiency of RET η_1 [, η_2] [%]	
Sample	UCNPs only		UCNPs + RoseB + PB		UCNPs + RoseB + PB		UCNPs + RoseB + PB	UCNPs + RoseB + PB
	550 nm	580 nm	550 nm	580 nm	550 nm	580 nm		
…@Er	710 ± 0.7	-	727 ± 0.6	600 ± 0.5	684 ± 0.3	-	-2,39	3,66
Yb@Er	665 ± 0.3	-	644 ± 0.3	556 ± 1.4	625 ± 0.6	-	3,16	6,02
Yb@YbEr	163 ± 0.2 (89 %)	-	163 ± 0.3 (92 %)	137 ± 0.5 (96 %)	152 ± 0.3 (89 %)	-	0,00	6,75
	711 ± 4.8	-	751 ± 9.1	596 ± 23	723 ± 6	-	-5,63	-1,69

Table S6 Comparison of rise times and LRET efficiencies for …@Er, Yb@Er and Yb@YbEr UCNPs with RB anchored on their surface. The concentration of a dye was different in every sample and was chosen based on the highest Rose Bengal emission intensity

	Rise time [µs]						Efficiency base on Rise time [%]	
Sample	UCNPs only		UCNPs + RoseB		UCNPs + RoseB + PB		UCNPs + RoseB	UCNPs + RoseB + PB
	540 nm	580 nm	540 nm	580 nm	540 nm	580 nm	540 nm	580 nm
…@Er	1987 ± 110	-	1164 ± 45	1529 ± 64	2051 ± 107	-	41,42	-3,22
Yb@Er	1172 ± 35	-	1464 ± 49	1471 ± 58	1386 ± 46	-	-24,91	-18,26
Yb@YbEr	334 ± 4.3	-	329 ± 4.0	293 ± 32	309 ± 3.5	-	1,50	7,49

Table S7 Comparison of rose bengal concentration dependent decay times monitored at 540 nm emission under 976 nm photoexcitation. The bi-exponential decay model was used everywhere, where single-exponent was not sufficient to fit data reasonably

Decay time τ_1 [, τ_2] [µs]												
RB [µM]	Yb@Yb, Er (0.1%)		Yb@Yb, Er (0.2%)		Yb@Yb,Er (0.5%)		Yb@Yb,Er (3%)		Yb@Yb,Er (4%)		Yb@Yb,Er (5%)	
	τ_1 [µs]	τ_2 [µs]	τ_1 [µs]	τ_2 [µs]	τ_1 [µs]	τ_2 [µs]	τ_1 [µs]	τ_2 [µs]	τ_1 [µs]	τ_2 [µs]	τ_1 [µs]	τ_2 [µs]
0	405	-	373.0	-	305.0	-	183.0	453.0	184.0	403.0	146.0	399.0
2.9	226	-	354.0	-	321.0	-	184.0	426.0	186.0	399.0	134.0	391.0
9.8	376	-	360.0	-	310.0	-	182.0	445.0	169.0	379.0	138.0	394.0
29.5	368	-	350.0	-	313.0	-	184.0	405.0	162.0	375.0	154.0	406.0
98.3	226	-	336.0	-	338.0	-	183.0	397.0	151.0	362.0	142.0	388.0
294.8	224	-	328.0	-	342.0	-	227.0	429.0	155.0	359.0	174.0	409.0

Table S7a Comparison of LRET efficiencies (based on Table S7) monitored at 540 nm emission under 976 nm photoexcitation

Efficiency of RET η_1 [, η_2] [%]												
RB [µM]	Yb@Yb, Er (0.1%)		Yb@Yb, Er (0.2%)		Yb@Yb,Er (0.5%)		Yb@Yb,Er (3%)		Yb@Yb,Er (4%)		Yb@Yb,Er (5%)	
	η_1 [%]	η_2 [%]	η_1 [%]	η_2 [%]	η_1 [%]	η_2 [%]	η_1 [%]	η_2 [%]	η_1 [%]	η_2 [%]	η_1 [%]	η_2 [%]
0.00	-	-	-	-	-	-	-	-	-	-	-	-
2.90	44.20	-	5.09	-	-5.25	-	-0.55	5.96	-1.09	0.99	8.22	2.01
9.80	7.16	-	3.49	-	-1.64	-	0.55	1.77	8.15	5.96	5.48	1.25
29.50	9.14	-	6.17	-	-2.62	-	-0.55	10.60	11.96	6.95	-5.48	-1.75
98.30	44.20	-	9.92	-	-10.82	-	0.00	12.36	17.93	10.17	2.74	2.76
294.80	44.69	-	12.06	-	-12.13	-	-24.04	5.30	15.76	10.92	-19.18	-2.51

References:

1 I. Medintz and N. Hildebrandt, *FRET – Förster Resonance Energy Transfer*, .

2 J.-C. G. Bünzli and S. V. Eliseeva, Springer-Verlag, 2010, vol. 7, pp. 1–45.

3 -L K Wong, P. A. Tanner, H. Kong, B. University, S. P. A. Tanner, P. A. Tanner, L. Zhou, C. Duan and K.-L. Wong, *This J. is Cite this Chem. Soc. Rev*, 2018, **47**, 5234.

4 S. Melle, O. G. Calderóncalderón, M. Laurenti, D. Mendez-Gonzalez, A. Egatz-Gómezgómez, E. Lópezlópez-Cabarcos, E. Cabrera-Granado, E. Díaz and J. Rubio-Retama, *J. Phys. Chem. C*, 2018, **122**, 40.

5 L. Mattsson, K. D. Wegner, N. Hildebrandt and T. Soukka, *RSC Adv.*, 2015, **5**, 13270–13277.

6 S. Diao, H. Dai, N. J. J. Johnson, A. Almutairi, E. M. Chan and S. He, *J. Am. Chem. Soc.*, 2017, **139**, 3275–3282.

7 S. Prahl, Optical absorption spectrum of Rose bengal in basic ethanol, https://omlc.org/spectra/PhotochemCAD/data/084-abs.txt, (accessed 26 February 2020).

8 D. Wawrzyńczyk, U. Bazylińska, Ł. Lamch, J. Kulbacka, A. Szewczyk, A. Bednarkiewicz, K. A. Wilk and M. Samoć, *ChemSusChem*, 2019, **12**, 706–719.

9 A. López de Guereñu, P. Bastian, P. Wessig, L. John and M. U. Kumke, *Biosensors*, 2019, **9**, 9.

10 F. T. Rabouw, P. T. Prins, P. Villanueva-Delgado, M. Castelijns, R. G. Geitenbeek and A. Meijerink, *ACS Nano*, 2018, **12**, 4812–4823.

11 V. I. Sokolov, A. V Zvyagin, S. M. Igumnov, S. I. Molchanova, M. M. Nazarov, A. V Nechaev, A. G. Savelyev, A. A. Tyutyunov, E. V Khaydukov and V. Ya Panchenko, *Opt. Spectrosc.*, 2015, **118**, 637–642.

12 V. Muhr, C. Würth, M. Kraft, M. Buchner, A. J. Baeumner, U. Resch-Genger and T. Hirsch, *Anal. Chem.*, 2017, **89**, 4868–4874.

13 W. Sun, L. Luo, Y. Feng, Y. Qiu, C. Shi, S. Meng, X. Chen and H. Chen, *Adv. Mater.*, , DOI:10.1002/adma.202000377.

14 M. Tarai and A. K. Mishra, *Anal. Chim. Acta*, 2016, **940**, 113–119.